

Orbital angular momentum of spatiotemporal vortices: a ray-mechanical analogy

Sophie Vo,¹ Konstantin Y. Bliokh,^{2,3,4} and Miguel A. Alonso^{5,1}

¹*The Institute of Optics, University of Rochester, Rochester, NY 14627, USA*

²*Donostia International Physics Center (DIPC), Donostia-San Sebastián 20018, Spain*

³*IKERBASQUE, Basque Foundation for Science, Bilbao 48009, Spain*

⁴*Centre of Excellence ENSEMBLE3 Sp. z o.o., 01-919 Warsaw, Poland*

⁵*Aix Marseille Univ, CNRS, Centrale Med, Institut Fresnel, UMR 7249, Marseille Cedex 20, 13397, France*

Spatiotemporal vortex pulses (STVPs) are wavepackets that carry transverse orbital angular momentum (OAM), whose proper quantification has been the subject of recent debate. In this work, we introduce a simplified mechanical model of STVPs, consisting of a loop of non-interacting point particles traveling at a uniform constant speed but at slightly different angles. We examine different initial conditions for the particle loop, including configurations that are elliptic in space at a given time and configurations that are elliptic in spacetime at a fixed propagation distance. Furthermore, employing a non-uniform mass distribution allows the particle loop to mimic the STVP not only in configuration space but also in momentum space. Remarkably, when supplemented by a semiclassical vorticity quantization condition, our mechanical model exactly reproduces different wave-based OAM results previously reported for paraxial STVPs.

I. INTRODUCTION

Wave vortices are fundamental structures in inhomogeneous wave fields of any nature, both classical [1, 2] and quantum [3]. These are characterized by phase singularities, i.e., points of vanishing intensity with dislocations of the wavefront [4]. For localized wave beams or packets, wave vortices are also commonly associated with the *orbital angular momentum (OAM)* carried by the wave [5–8].

Until fairly recently, most studies of wave vortices focused on monochromatic waves and stationary vortices. In particular, axially symmetric vortex beams support vortices whose normalized OAM is directed along the beam axis (i.e., along the mean wave momentum) and is unambiguously quantified (for scalar waves) by the integer vortex strength ℓ [5, 7, 9, 10]. Notably, this *longitudinal OAM* is purely *intrinsic*, i.e., invariant with respect to the choice of coordinate origin [7, 11].

In the more general case of non-monochromatic waves, vortices can be non-stationary, as already recognized in the pioneering work of Nye and Berry [4]. Recently, such *spatiotemporal vortices* have attracted considerable attention, motivating theoretical [12–20] and experimental [21–28] studies across optical, acoustic, quantum, and water-wave systems.

Localized spatiotemporal vortices, referred to as *spatiotemporal vortex pulses (STVPs)*, carry OAM that is not aligned with the mean momentum [7, 13]. In the limiting case of the vortex moving orthogonally to the wavefront dislocation line, the OAM becomes purely *transverse* [14, 15, 17, 20, 22].

Remarkably, theoretical calculations of such transverse OAM encountered significant controversies and debated the magnitude of the transverse OAM carried by STVPs [14, 15, 17, 20, 29–31]. The main origin for these discrepancies lies in the strong dependence of transverse OAM

TABLE I. Expressions for the transverse OAM of STVPs in prior art. Here, ℓ is the STVP's topological charge and γ is the ratio of the longitudinal and transverse dimensions of the STVP.

Reference	OAM
Bliokh [15], <i>xz</i> framework and	$L_y = \frac{\gamma}{2} \ell$ $L_y^{\text{INT}} = \frac{\gamma + \gamma^{-1}}{2} \ell$
Bekshaev [20], <i>xt</i> framework	$L_y^{\text{EXT}} = -\frac{1}{2\gamma} \ell$
Hancock <i>et al.</i> [14], <i>xt</i> framework	$L_y = \frac{\gamma}{2} \ell$
	$L_y^{\text{INT}} = \frac{\gamma}{2} \ell$
Porras [17], <i>xt</i> framework	$L_y^{\text{EXT}} = -\frac{\gamma}{2} \ell$ $L_y = 0$

on the choice of coordinate origin, which implies an essential *extrinsic* OAM part [7, 15]. Differing results have been obtained for the OAM and its intrinsic and extrinsic parts, as summarized in Table I. It has been suggested that these discrepancies originate from the choice of STVP's shape and reference point.

Here we re-examine the transverse OAM of STVPs, using an approach that differs substantially from the methods used in previous studies. Instead of relying on a *wave-based* analysis, we put forward a simplified *mechanical* model similar to the geometrical ray approach. Despite its simplicity, this model reproduces the main results of prior wave calculations and provides an intuitive framework that sheds light on the origins of the previously-reported differences.

II. MODEL OF A STVP AS A PARTICLE LOOP WITH UNIFORM MASS DENSITY

A. xz and xt frameworks for elliptical STVPs

STVPs are wavepackets that can be seen as propagating in space and evolving in time. It was recently shown that the diffractive deformation of STVPs with propagation can be understood by considering a non-interacting set of particles, each running with the same speed c along a rectilinear trajectory referred to here as a *ray* [18], as illustrated in Fig. 1. Each ray in the set corresponds to a value of a periodic parameter $\xi \in [0, 2\pi]$. Assuming a STVP propagating in the (x, z) plane along the z -axis, the coordinates of each particle can be written in the following form:

$$\mathbf{r}(\xi, t) = \begin{pmatrix} X_0(\xi) \\ Z_0(\xi) \end{pmatrix} + [t - t_0(\xi)] c \mathbf{u}(\xi), \quad (1)$$

where $\mathbf{u}(\xi)$ is a unit vector defining the direction of each ray:

$$\mathbf{u}(\xi) = \frac{1}{\sqrt{1 + \Delta_x^2 \cos^2 \xi}} \begin{pmatrix} \Delta_x \cos \xi \\ 1 \end{pmatrix} \simeq \begin{pmatrix} \Delta_x \cos \xi \\ 1 \end{pmatrix}. \quad (2)$$

Here, Δ_x is the maximal magnitude of the ray slope with respect to the z axis, and the linear approximation in $\Delta_x \ll 1$ in the second step corresponds to the paraxial approximation.

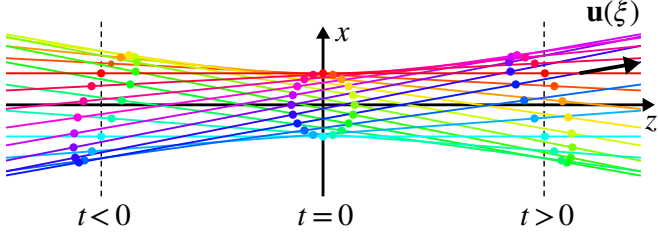


FIG. 1. Rays corresponding to trajectories of particles for modeling the evolution of STVPs [18]. In all figures, hue colors are used to identify the value of $\xi \in [0, 2\pi]$ for the corresponding ray.

The functions X_0 , Z_0 and t_0 in Eq. (1) determine the initial conditions (and by consequence the general shape) of the set of particles. Note that one of them is redundant, but using all three simplifies the analysis that follows. We now consider two particular choices:

xz STVPs: In the first framework, we consider the following initial conditions:

$$X_0(\xi) = w_x \sin \xi, \quad Z_0(\xi) = w_z \cos \xi, \quad t_0(\xi) = 0. \quad (3)$$

These conditions are such that the particles trace over the xz plane at $t = 0$ an ellipse of semi-axes w_z and w_x centered at the origin, as shown in Fig. 2(c). The

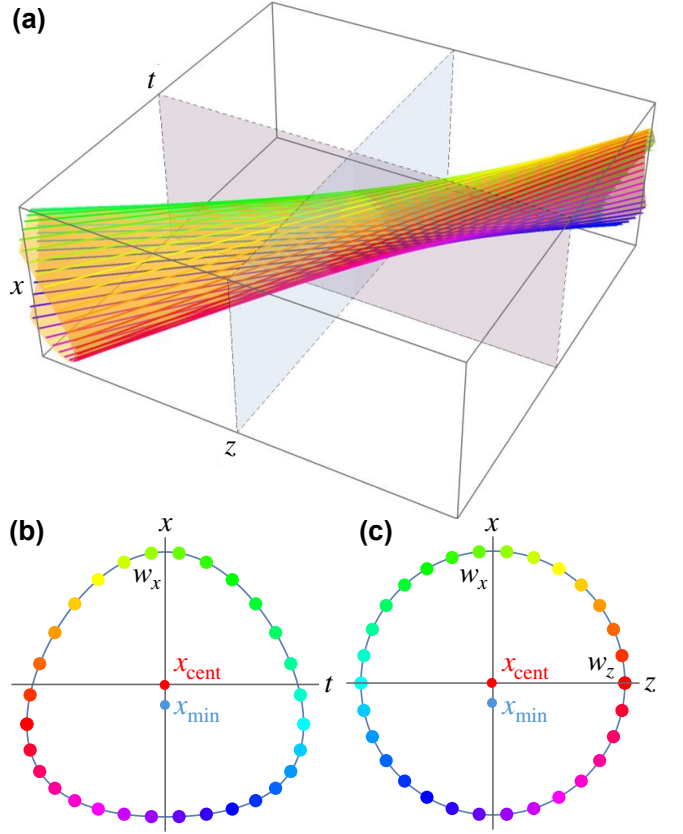


FIG. 2. Ray-optics modeling of xz STVPs: (a) Ray bundle in space and time for $w_x = w_z$ and $\Delta_x = 0.3$; (b,c) Cross-sections at $z = 0$ (b), and $t = 0$ (c), where the reference points x_{cent} and x_{min} are also indicated.

substitution of initial conditions (3) into Eq. (1) can be used to define a parameterized surface in spacetime, as illustrated in Fig. 2(a). Note from Fig. 2(b) that the cross-section of this surface by the xt -plane at $z = 0$ is not elliptic. The propagation of the particles is also illustrated in Supplementary Movie 1.

xt STVPs: In the second framework, we choose instead the initial conditions

$$X_0(\xi) = w_x \sin \xi, \quad Z_0(\xi) = 0, \quad t_0(\xi) = -\frac{w_t}{c} \cos \xi. \quad (4)$$

In contrast with the previous case, these conditions guarantee that the particles trace at $z = 0$ an ellipse of semi-axes w_x and w_t/c centered at the origin over the xt -plane, as illustrated in 3(c). Similarly to the previous case, the parameterized surface defined by Eq. (1) with initial conditions (4) can be plotted in spacetime, as shown in Fig. 3(a). We see from Fig. 3(c) that the cross-section of this spacetime surface by the xz -plane at $t = 0$ has a non-elliptical shape. The propagation of the particle loop is illustrated in Supplementary Movie 2.

We note that the simple ray-optical profiles in Figs. 2(b,c) and 3(b,c) resemble the shapes of the wave-based calculations by Porras [29], which used elliptical intensity distributions either in the (x, z) plane or in the

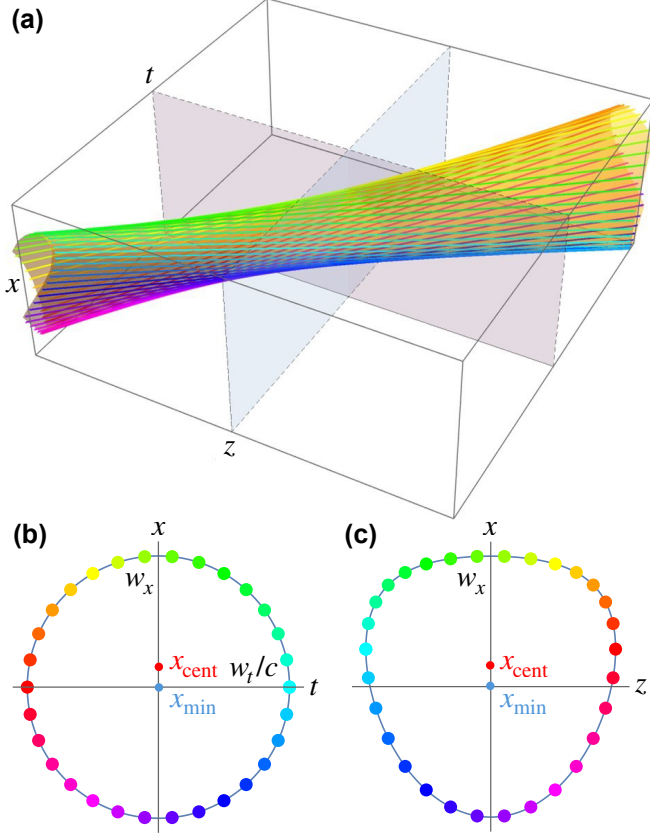


FIG. 3. Ray-optics modeling of xt STVPs: (a) Ray bundle in space and time for $w_x = w_t$ and $\Delta_x = 0.3$; (b,c) Cross-sections at $z = 0$ (b), and $t = 0$ (c), where the reference points x_{cent} and x_{min} are also indicated.

(x, t) plane.

B. Orbital angular momentum

We now compare these two frameworks and calculate the OAM for the corresponding particle loops. We start by assuming classical particles of the same mass propagating at the same speed, and hence carrying linear momentum density (in terms of the parameter ξ)

$$\mathbf{p}(\xi) = \frac{mc}{2\pi} \mathbf{u}(\xi), \quad (5)$$

where m is the total mass of the set of particles. Then, the OAM computed with respect to a chosen point $\mathbf{r}_0 = (0, x_0)$ at the $z = 0$ plane is defined by

$$\langle \mathbf{L} \rangle(x_0) = \int_0^{2\pi} [\mathbf{r}(\xi, t) - \mathbf{r}_0] \times \mathbf{p}(\xi) d\xi. \quad (6)$$

It is easy to see from Eqs. (1) and (5) that the OAM (6) is independent of t (so it is sufficient to set $t = 0$), it is directed along the y axis (normal to the zx -plane),

and its magnitude depends on the choice of the reference position x_0 .

Substituting Eqs. (1)–(4) into Eq. (6), we find that the OAM of an STVP in the xz and xt frameworks are given (in the paraxial regime) by

$$\begin{aligned} \langle L_y^{(xz)} \rangle(x_0) &= mc \left(x_0 + \frac{\Delta_x w_z}{2} \right), \\ \langle L_y^{(xt)} \rangle(x_0) &= mc x_0. \end{aligned} \quad (7)$$

In order to calculate an “intrinsic” OAM, one has to choose an appropriate x_0 not simply as the origin, but according to some meaningful criterion in this mechanical analogy. We consider the following two options:

- the transverse centroid of the particles at $t = 0$, defined by

$$x_{\text{cent}} = \frac{1}{2\pi} \int_0^{2\pi} x(\xi, t = 0) d\xi; \quad (8)$$

- the point $(0, x_{\text{min}})$ that minimizes the square of the OAM [32]. More specifically, x_{min} is the value of x_0 that minimizes the quantity

$$\langle L^2 \rangle(x_0) = \frac{m^2 c^2}{2\pi} \int_0^{2\pi} |[\mathbf{r}(\xi, t = 0) - \mathbf{r}_0] \times \mathbf{u}(\xi)|^2 d\xi. \quad (9)$$

The exact expressions (valid in the nonparaxial regime) for the different centroids and the corresponding OAM are summarized in the tables in the Supplementary Document A. In the paraxial regime, linear in $\Delta_x \ll 1$, we obtain for the xz and xt STVPs the centroids and corresponding OAM (7) summarized in Table II. Notably, the OAM values evaluated either at x_{cent} or x_{min} are similar in the paraxial regime for both types of STVP: xz -elliptical and xt -elliptical. Thus, for this simple particle model, shape itself is not the source of discrepancy between different results when considering the paraxial regime, as long as OAM calculations use a meaningful reference point. A discrepancy arrives, on the other hand, if the reference point is simply the origin.

In the next section, we refine these results by leveraging a “wavization” of the particle model, to express them as a function of the STVP’s topological charge ℓ .

C. Quantization of vorticity

In order to relate the obtained OAM to a topological charge, one must perform a semi-classical quantization based on assigning phases along the rays according to their optical path length (OPL). The phase for each ray at the particle’s position, referred to here as $\Phi(\xi)$, must

TABLE II. Centroids and corresponding OAM for the xz -elliptic and xt -elliptic STVPs in the uniform-mass model.

Quantity	xz STVP	xt STVP
x_{cent}	0	$\frac{\Delta_x w_t}{2}$
x_{min}	$-\frac{\Delta_x w_z}{2}$	0
$\langle L_y \rangle(x_{\text{cent}})$	$mc \frac{\Delta_x w_z}{2}$	$mc \frac{\Delta_x w_t}{2}$
$\langle L_y \rangle(x_{\text{min}})$	0	0

be chosen to guarantee phase consistency between neighboring rays. This phase satisfies the following differential equation:

$$\frac{\partial \Phi(\xi)}{\partial \xi} = k_0 \mathbf{u}(\xi) \cdot \frac{\partial \mathbf{r}(\xi, t)}{\partial \xi}. \quad (10)$$

where $k_0 = mc$ is the wavenumber corresponding to the classical momentum of the particles. It is easy to show from Eqs. (1) and (2) that the right-hand side of this equation is independent of t . Without loss of generality, we choose $\Phi(0) = 0$. Rigorous solutions to Eq. (10) are given in the Supplementary Document B for the particle loops in the xz and xt frameworks. Since the ray family is periodic, the ray construction is self-consistent from the wave-optical point of view only if the values of Φ for $\xi = 0$ and $\xi = 2\pi$ (corresponding to the same ray) lead to consistent phases. That is, the condition $\Phi(2\pi) = 2\pi\ell$ must be satisfied, where ℓ is an integer (corresponding to the STVP's topological charge). Since the underlying ray bundles are the same, this quantization leads to the same restriction for both frameworks, which in the paraxial regime takes the simple form

$$k_0 \Delta_x w_x = 2\ell. \quad (11)$$

Using the quantization relation (B6), the results of Table II can be expressed in terms of the topological charge ℓ , as well as of the ellipses' semiaxis ratios $\gamma = w_z/w_x$ (for xz STVPs) and $\gamma = w_t/w_x$ (for xt STVPs), as given in Table III. Surprisingly, these results with respect to either of the two centroids do not agree with any of the results for the intrinsic OAM in Table I. Curiously, for $\gamma = 1$, the OAM with respect to x_{cent} yields $\langle L_y \rangle = \ell$, the well-known formula for monochromatic spatial vortices [5–7]. The origin of this discrepancy will be clarified in Section III.

D. Wave estimates through Gaussian wavepacket superposition

One can estimate STVP wavefields from the particle-ray model by “sewing the wave flesh on the classical

TABLE III. OAM from Table II after the vortex quantization.

Quantity	xz STVP	xt STVP
$\langle L_y \rangle(x_{\text{cent}})$	$\gamma\ell$	$\gamma\ell$
$\langle L_y \rangle(x_{\text{min}})$	0	0

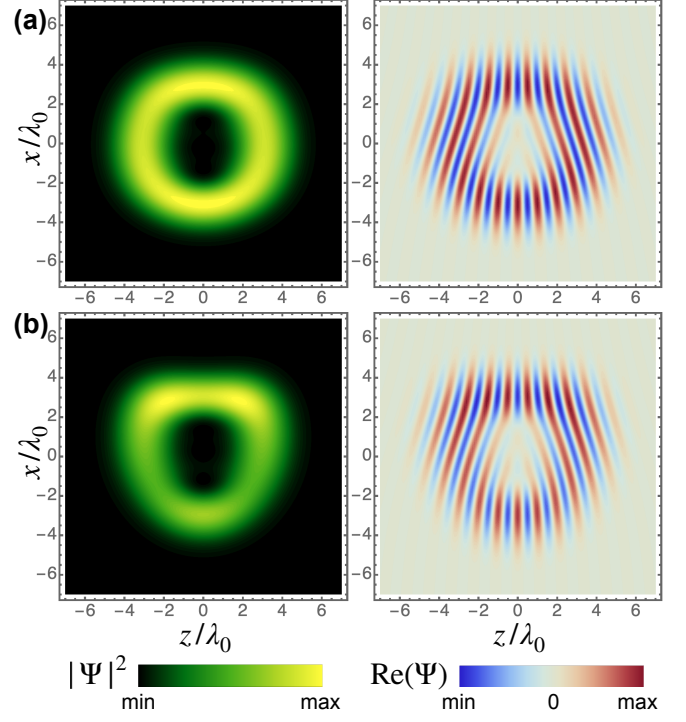


FIG. 4. Intensity and real part of the wavefield $\Psi(x, z, 0)$, Eq. (12), for an xz STVP (a) and an xt STVP (b) with topological charge $\ell = 3$, directional spread $\Delta_x = 0.3$, and widths $w_x = w_z = w_t = 3.29\lambda_0$ ($\gamma = 1$), where $\lambda_0 = 2\pi/k_0$. The axes are in units of λ_0 .

bones” [33, 34]. For this, we dress each particle with a Gaussian wavepacket traveling in the direction of the ray. The wave field at $t = 0$ can be approximately written as

$$\Psi(x, z, 0) = \int_0^{2\pi} e^{-\frac{[x - X(\xi, 0)]^2 + \gamma^{-2}[z - Z(\xi, 0)]^2}{2w_{\text{dress}}^2}} \times e^{i\Phi(\xi) + i k_0 \{[x - X(\xi, 0)]u_x(\xi) + [z - Z(\xi, 0)]u_z(\xi)\}} d\xi, \quad (12)$$

where w_{dress} is the width of each Gaussian wavepacket, chosen here as $w_{\text{dress}} = (w_x/k_0 \Delta_x)^{1/2}$. Figure 4 shows the intensity and real part of an xz STVP and an xt STVP with topological charge $\ell = 3$. Note that the global shapes of these intensity profiles are qualitatively consistent with those for the particle loops in Figs. 2(c) and 3(c), as well as with wave solutions [29]. Note also that the wavefront spacing is fairly uniform over the whole pulse.

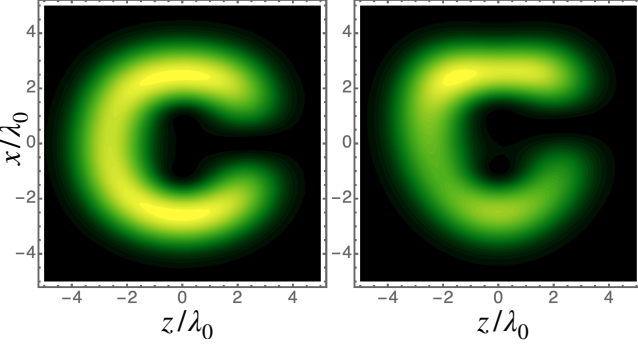


FIG. 5. Effect of the non-satisfaction of the quantization condition, $\Phi(2\pi) = 2\pi\ell$, on the wavefield intensity of an xz STVP (left) and an xt STVP (right), for $\Delta_x = 0.3$ and $w_x = w_z = w_t = 2.8\lambda_0$, which give $\Phi(2\pi)/2\pi = 2.64$. The positions of the interruptions depend on the chosen region of integration, in this case $\xi \in [0, 2\pi]$.

The quantization condition $\Phi(2\pi) = 2\pi\ell$ guarantees that the integrand in (12) is periodic, so the integral is independent of the choice of limits as long as the interval covers the complete loop. If we choose particle loop dimensions for which $\Phi(2\pi)$ is not an integer multiple of 2π , on the other hand, the STVP intensity profile does not close properly due to a phase inconsistency at the limits of integration, as shown on Fig. 5. Such wavefields can model *fractional STVPs* [35], analogous to the previously studied fractional spatial vortices [36, 37].

III. RAY-PARTICLE MODEL WITH A NON-UNIFORM MASS DENSITY

A. Mimicking wave momenta

In order to understand the discrepancy between the results in Tables I and III, we consider the correspondence between rays and plane waves in the wave spectrum. In this manner the elliptical initial distribution of particles in the (x, z) or (x, t) plane corresponds to the elliptical distribution of the wave spectrum in the (k_x, k_z) or (k_x, ω) plane [15]. Importantly, these distributions involve plane waves with different frequencies and wavenumbers, i.e., *energies and momentum magnitudes*, while the simple ray-mechanical model of Section II assumes particles with equal energies and momentum magnitudes. This discrepancy can be resolved by introducing a nonuniform mass distribution for the classical particles, which modifies their energy and momentum-magnitude distributions in a proportional manner, similar to frequencies and wavenumbers of relativistic particles (photons). We therefore consider a ray family with momentum distribution $\mathbf{p}(\xi)$ mimicking the elliptical wavevector

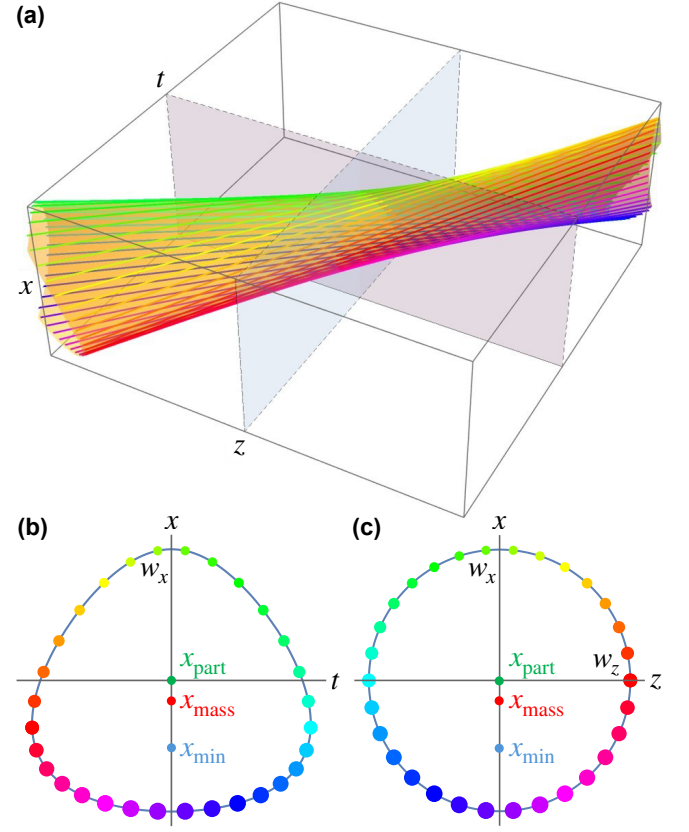


FIG. 6. Ray-optics modeling of xz STVPs with non-uniform particle mass density (indicated by the particles' sizes): (a) Ray bundle in space and time with $w_x = w_z$ and $\Delta_x = \Delta_z = 0.3$; (b,c) Cross-sections at $z = 0$ (b), and $t = 0$ (c), where the reference points x_{mass} , x_{part} and x_{min} are also indicated.

distribution in [15]:

$$\mathbf{p}(\xi) = \frac{mc}{2\pi} \begin{pmatrix} \Delta_x \cos \xi \\ 1 - \Delta_z \sin \xi \end{pmatrix}. \quad (13)$$

In the paraxial regime, $(\Delta_x, \Delta_z) \ll 1$. That is, keeping the particles' speed c as constant, we have a mass density proportional to $|\mathbf{p}(\xi)|$. Note that the corresponding unit vectors slightly differ from those in Eq. (2) but coincide with them in the paraxial regime:

$$\mathbf{u}(\xi) = \frac{\mathbf{p}(\xi)}{|\mathbf{p}(\xi)|} \simeq \begin{pmatrix} \Delta_x \cos \xi \\ 1 \end{pmatrix}. \quad (14)$$

We keep the same initial conditions as in Section II A: Eqs. (3) for xz STVPs and (4) for xt STVPs. Figures 6 and 7 are then the counterparts of Figs. 2 and 3 with the slightly modified ray directions in Eqs. (13) and (14). Supplementary Movies 3 and 4 illustrate the corresponding propagation of the particle loops.

Two observations can be made. First, the non-elliptical shapes in Figs. 6(b) and 7(c) differ slightly from the non-elliptical shapes in Figs. 2(b) and 3(c), while still being similar to the wave-intensity shapes in [29]. Second, the

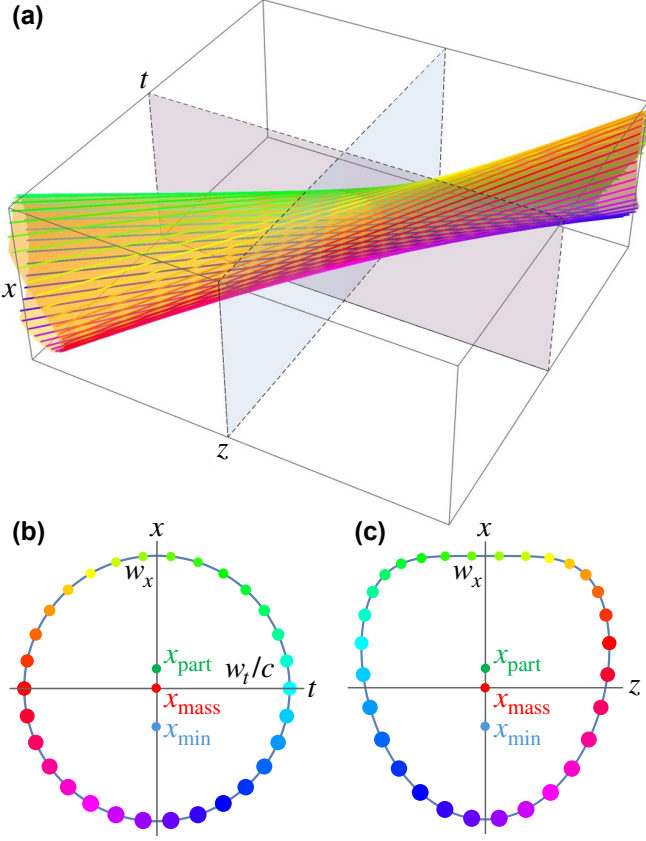


FIG. 7. Ray-optics modeling of xt STVPs with non-uniform particle mass density (indicated by the particles' sizes): (a) Ray bundle in space and time with $w_x = w_t$ and $\Delta_x = \Delta_z = 0.3$; (b,c) Cross-sections at $z = 0$ (b), and $t = 0$ (c), where the reference points x_{mass} , x_{part} and x_{min} are also indicated.

dot size in Figs. 6 and 7 is proportional to the corresponding non-uniform mass density. This varying mass density causes a shift of the effective mass/energy centroid.

B. Orbital angular momentum

We compare again the xz and xt STVP frameworks by computing their OAM. Substituting Eqs. (1)–(4) and (13) into Eq. (6), we find that the OAM in both the xz and xt frameworks are given in the paraxial regime by [cf. Eqs. (7)]:

$$\begin{aligned} \langle L_y^{(xz)} \rangle(x_0) &= mc \left(x_0 + \frac{\Delta_z w_x + \Delta_x w_z}{2} \right), \\ \langle L_y^{(xt)} \rangle(x_0) &= mc \left(x_0 + \frac{\Delta_z w_x}{2} \right). \end{aligned} \quad (15)$$

That is, in both frameworks the non-uniformity of the particles' mass density (proportional to Δ_z) causes an increase by $mc\Delta_z w_x/2$.

Similarly to Section II, these new OAM expressions can be computed for different centroids x_0 . While the

centroid that minimizes the squared OAM, x_{min} , is still defined by Eq. (9), the particle-beam centroid can now be defined in two ways:

- First, one can calculate the *mass centroid* (which corresponds to the wavepacket's *energy centroid*), which takes into account their nonuniform ξ -distributions:

$$x_{\text{mass}} = \frac{1}{mc} \int_0^{2\pi} x(\xi, t) |\mathbf{p}(\xi)| d\xi. \quad (16)$$

It is easy to show that this expression is time-independent, and one can use $|\mathbf{p}(\xi)| \simeq (mc/2\pi)(1 - \Delta_z \sin \xi)$ in the paraxial approximation.

- Second, one can use the geometric *particle centroid*, weighted not by mass/energy density but by particle number density [15, 38]. This centroid is defined similarly to Eq. (8):

$$x_{\text{part}} = \frac{1}{2\pi} \int_0^{2\pi} x(\xi, t) d\xi. \quad (17)$$

The centroid (17) is time-independent in our model. Note, however, that in nonparaxial wave solutions [29, 39, 40] the particle centroid $\mathbf{r}_{\text{part}}(t)$ can propagate along a straight line that is non-collinear with the mean momentum, which would result in non-conservation of the OAM defined with respect to such time-varying centroid $x_{\text{part}}(t)$.

Table IV summarizes the paraxial results for the OAM for the three different reference points in the xz and xt frameworks. Again, we note that these paraxial OAM calculations are independent of the particular model (xz or xt) used for the particle loop. We also observe that the result for $\langle L_y \rangle(x_{\text{mass}})$ is fully consistent with $\langle L_y \rangle(x_{\text{cent}})$ in Table II, while $\langle L_y \rangle(x_{\text{part}})$ picks up an extra term proportional to Δ_z . On the other hand, the use of a nonuniform mass distribution does cause a change in the result for $\langle L_y \rangle(x_{\text{min}})$ with respect to that in Table II. However, all results in Table IV are fully consistent with those in Table II in the limit $\Delta_z \rightarrow 0$.

C. Quantization of vorticity

We again can express the OAM in terms of the topological charge ℓ by discretizing the phase accumulated over the loop. However, the use of a non-uniform momentum density translates in the wave domain to using a wavevector $\mathbf{k}(\xi) = k_0(2\pi/mc)\mathbf{p}(\xi) = 2\pi\mathbf{p}(\xi)$, whose non-uniform magnitude is centered at k_0 . We then consider a phase Φ defined similar to Eq. (10):

$$\frac{\partial \Phi(\xi)}{\partial \xi} = \mathbf{k}(\xi) \cdot \frac{\partial \mathbf{r}(\xi, t)}{\partial \xi}. \quad (18)$$

TABLE IV. Centroids and corresponding OAM for the xz -elliptic and xt -elliptic STVPs in the nonuniform-mass model.

Quantity	xz STVP	xt STVP
x_{mass}	$-\frac{\Delta_z w_x}{2}$	$\frac{\Delta_x w_t - \Delta_z w_x}{2}$
x_{part}	0	$\frac{\Delta_x w_t}{2}$
x_{min}	$-\Delta_z w_x - \frac{\Delta_x w_z}{2}$	$-\Delta_z w_x$
$\langle L_y \rangle(x_{\text{mass}})$	$mc \frac{\Delta_x w_z}{2}$	$mc \frac{\Delta_x w_t}{2}$
$\langle L_y \rangle(x_{\text{part}})$	$mc \frac{\Delta_z w_x + \Delta_x w_z}{2}$	$mc \frac{\Delta_z w_x + \Delta_x w_t}{2}$
$\langle L_y \rangle(x_{\text{min}})$	$-mc \frac{\Delta_z w_x}{2}$	$-mc \frac{\Delta_z w_x}{2}$

Integrating Eq. (18) in the paraxial approximation and imposing the quantization condition $\Phi(2\pi) = 2\pi\ell$, we obtain similar results in the xz and xt frameworks:

$$k_0(\Delta_x w_x + \Delta_z w_{z,t}) = 2\ell. \quad (19)$$

This quantization condition differs from that in Eq. (B6) through the appearance of a term proportional to Δ_z , related to the non-uniform weight of the particles.

Similarly to Section II, we introduce the ratio of the STVP ellipse semiaxes in real space, $\gamma = w_z/w_x = w_t/w_x$, which should also correspond to the inverted relation for the momentum-space ellipse in Eq. (13): $\Delta_z/\Delta_x = 1/\gamma$. Using this parameter and the quantization condition (19), we re-write the OAM from Table IV in Table V.

Remarkably, the resulting expressions precisely reproduce the results obtained in [14–16, 20] and shown in Table I. First, the OAM with respect to the mass centroid coincides with $L_y = \gamma\ell/2$ in [14, 15, 20, 39] and $L_y^{\text{INT}} = \gamma\ell/2$ in [17, 29] (all these results were calculated with respect to the electromagnetic-energy centroid). This OAM is half-integer for a circular STVP with $\gamma = 1$. Second, the OAM with respect to the particle centroid coincides with $L_y^{\text{INT}} = (\gamma + \gamma^{-1})\ell/2$ calculated in [15, 20] with respect to the ‘photon-probability’ centroid. This OAM becomes integer for $\gamma = 1$ and has the same form as longitudinal OAM of monochromatic vortex beams.

D. Wave estimates

Wave estimates can be calculated by using (12) with the substitution $k_0 \mathbf{u}(\xi) \rightarrow \mathbf{k}(\xi) = 2\pi \mathbf{p}(\xi)$. Figure 8 shows the intensity and real part of, respectively, an xz STVP and an xt STVP with topological charge $\ell = 3$. Note that the global shapes of the intensity profiles in these figures are consistent with the ray loops of Figs. 6(c)

TABLE V. OAM from Table IV after the vortex quantization.

Quantity	xz STVP	xt STVP
$\langle L_y \rangle(x_{\text{mass}})$	$\frac{\gamma}{2}\ell$	$\frac{\gamma}{2}\ell$
$\langle L_y \rangle(x_{\text{part}})$	$\frac{\gamma + \gamma^{-1}}{2}\ell$	$\frac{\gamma + \gamma^{-1}}{2}\ell$
$\langle L_y \rangle(x_{\text{min}})$	$-\frac{1}{2\gamma}\ell$	$-\frac{1}{2\gamma}\ell$

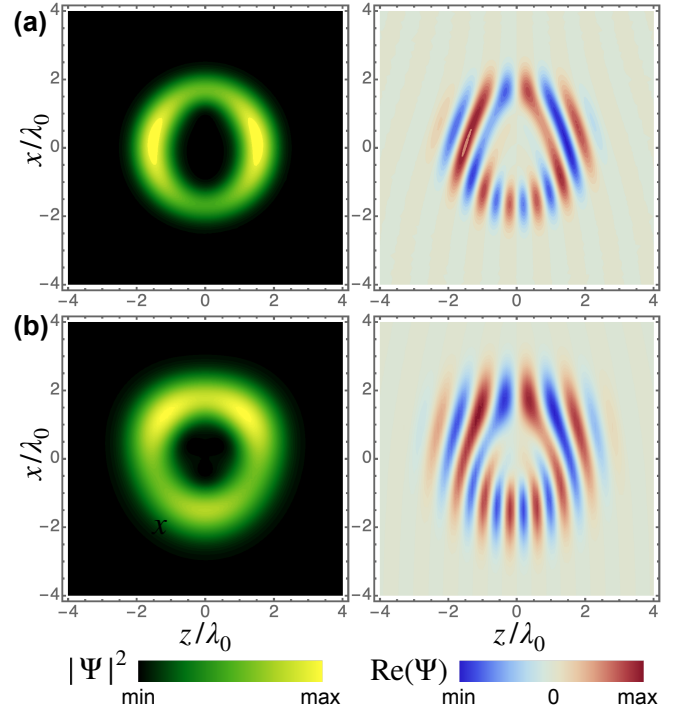


FIG. 8. Same as in Fig. 4 but for the model with a non-uniform mass distribution. The parameters are $\ell = 3$ and $w_x = w_z = w_t = 1.59\lambda_0$.

and 7(c). In addition, differently from the case for uniform mass density, the plots for the real part now show different wavefront spacings at the top and bottom of the STVP, reflecting the fact that local wavelength is inversely proportional to mass weight.

E. The role of dispersion

The OAM with respect to the mass centroid (16), $\langle L_y \rangle(x_{\text{mass}}) = \gamma\ell/2$ corresponds to the OAM of optical STVPs calculated with respect to the energy centroid [14, 15, 20, 39]. For optical waves, which correspond to massless relativistic particles (photons), the energy, mass, and the absolute value of the momentum are all proportional to each other. This is expressed by the linear dispersion relation $\omega = kc$ or $E = pc = mc^2$.

Therefore, our model and the OAM expressions are also valid for other waves with linear dispersion, such as sound waves in a fluid or gas [15].

For waves with a nonlinear dispersion relation, this model and OAM equations are no longer valid. For example, let us consider STVPs of nonrelativistic quantum particles. The relation between the energy, mass, and momentum becomes $E \simeq mc^2 + p^2/2m$, where the second term is a small correction to the main rest energy. For such STVPs, the momentum distribution is still given by Eq. (13), but calculating the mass or energy centroid (16) we need to change $|\mathbf{p}(\xi)| \rightarrow mc/2\pi$. This results in the equivalence of the mass and particle centroids (as expected in nonrelativistic physics), $x_{\text{mass}} = x_{\text{part}}$, and a uniquely defined intrinsic OAM with respect to this center: $\langle L_y \rangle(x_{\text{mass}}) = (\gamma + \gamma^{-1})\ell/2$ [15].

IV. CONCLUDING REMARKS

We have presented a simple model using rays associated with the rectilinear paths of traveling particles to understand the OAM of STVPs. This model illustrates, for example, how STVPs can be elliptical either in space or in spacetime, but not in both simultaneously [29]. Deformations of the STVP in the (x, z) or (x, t) planes produce a shift of its centroid; however, once this shift is properly accounted for in the OAM calculations, the resulting OAM is independent of whether the STVP is elliptical in space or in spacetime.

We also considered two different models for the particle mass-density distribution: a uniform distribution and a non-uniform one chosen such that the mechanical momentum distribution mimics the spatial Fourier spectrum of a STVP. These different mass distributions do not affect the mechanical OAM calculated with respect to the mass centroid, at least within the paraxial regime (see Tables II and IV). The similarity of these mechanical results reflects the fact that, in all cases, the particle distribution undergoes similar evolutions in all cases, including an approximately quarter-cycle rotation (ignoring other deformations) between $t = 0$ and $|t| \rightarrow \infty$, as can be observed from the four Supplemental Movies. However, the choice of mass distribution does have an important effect in the semiclassical correspondence between particles and waves and in the resulting vortex quantization conditions, Eqs. (B6) and (19). Namely, for a given directional spread Δ_x , the spatial width w_x needed to achieve a given vorticity ℓ must be twice as large for the uniform

mass density as for the non-uniform one. This difference can be understood by looking at the real-part field plots in Figs. 4 and 8: for the latter (varying mass density), the different wavefront spacings on the top and bottom of the STVP naturally help accommodate a different number of fringes on both sides, so a given vorticity is achievable with a smaller loop.

Using the model with a non-uniform mass distribution and the corresponding quantization conditions, we were able to reproduce the results of previous wave-based calculations [14, 15, 17, 20, 29, 30] (see Tables I and V). This includes the differing values of the OAM computed with respect to the mass/energy centroid and the particle centroid. Notably, this distinction also depends on the wave dispersion and the associated relation between the momentum and energy of particles. In the present work, we employed a classical-particle model with a varying mass density to mimic the proportionality between momentum and energy characteristic of free-space optical (or sound) waves and relativistic massless particles. For other types of waves and dispersion relations, the model would need to be modified accordingly.

ACKNOWLEDGEMENTS

MAA acknowledges funding from the Agence Nationale de Recherche (ANR) through the project 3DPol, ANR-21-CE24-0014-01. KYB acknowledges support from Marie Skłodowska-Curie COFUND Programme of the European Commission (project HORIZON-MSCA-2022-COFUND-101126600-SmartBRAIN3), ENSEMBLE3 Project carried out within the International Research Agendas Programme (IRAP) of the Foundation for Polish Science co-financed by the European Union under the European Regional Development Fund (MAB/2020/14) and Teaming Horizon 2020 programme of the European Commission (GA. No. 857543), and Minister of Science and Higher Education “Support for the activities of Centers of Excellence established in Poland under the Horizon 2020 program” (contract MEiN/2023/DIR/3797).

We thank Miguel A. Porras and Etienne Brasselet for useful discussions. We would like to dedicate this work to the memory of Kevin J. Parker, whose enthusiasm for interesting wavepackets was contagious.

[1] M. S. Soskin and M. V. Vasnetsov, Singular optics, *Prog. Opt.* **42**, 219 (2001).

[2] M. R. Dennis, K. O’Holleran, and M. J. Padgett, Singular optics: Optical vortices and polarization singularities, *Prog. Opt.* **53**, 293 (2009).

[3] K. Y. Bliokh, I. P. Ivanov, G. Guzzinati, L. Clark, R. Van Boxem, A. Béché, R. Juchtmans, M. A. Alonso, P. Schattschneider, F. Nori, and J. Verbeeck, Theory and applications of free-electron vortex states, *Phys. Rep.* **690**, 1 (2017).

[4] J. F. Nye and M. V. Berry, Dislocations in wave trains, *Proc. R. Soc. Lond. A* **336**, 165 (1974).

[5] L. Allen, S. M. Barnett, and M. J. Padgett, *Optical Angular Momentum* (IoP Publishing, 2003).

[6] D. L. Andrews and M. Babiker, *The Angular Momentum of Light* (Cambridge University Press, Cambridge, England, UK, 2012).

[7] K. Y. Bliokh and F. Nori, Transverse and longitudinal angular momenta of light, *Phys. Rep.* **592**, 1 (2015).

[8] K. Y. Bliokh, Momentum, spin, and orbital angular momentum of electromagnetic, acoustic, and water waves, *Contemp. Phys.* **65**, 219 (2024).

[9] L. Allen, M. W. Beijersbergen, R. J. C. Spreeuw, and J. P. Woerdman, Orbital angular momentum of light and the transformation of Laguerre-Gaussian laser modes, *Phys. Rev. A* **45**, 8185 (1992).

[10] P. H. Ceperley, Rotating waves, *Am. J. Phys.* **60**, 938 (1992).

[11] M. V. Berry, Paraxial beams of spinning light, *Proc. of SPIE* **3487**, 6 (1998).

[12] A. P. Sukhorukov and V. V. Yangurova, Spatio-temporal vortices: properties, generation and recording, *Proc. SPIE* **5949**, 594906 (2005).

[13] K. Y. Bliokh and F. Nori, Spatiotemporal vortex beams and angular momentum, *Phys. Rev. A* **86**, 033824 (2012).

[14] S. W. Hancock, S. Zahedpour, and H. M. Milchberg, Mode structure and orbital angular momentum of spatiotemporal optical vortex pulses, *Phys. Rev. Lett.* **127**, 193901 (2021).

[15] K. Y. Bliokh, Orbital angular momentum of optical, acoustic, and quantum-mechanical spatiotemporal vortex pulses, *Phys. Rev. A* **107**, L031501 (2023).

[16] M. A. Porras, Propagation of higher-order spatiotemporal vortices, *Opt. Lett.* **48**, 367 (2023).

[17] M. A. Porras, Transverse orbital angular momentum of spatiotemporal optical vortices, *Prog. Electromagn. Res.* **177**, 95 (2023).

[18] S. Vo, R. Gutiérrez-Cuevas, and M. A. Alonso, Closed forms for spatiotemporal optical vortices and sagittal skyrmionic pulses, *J. Opt.* **26**, 95607 (2024).

[19] H. Wang, C. Guo, W. Jin, A. Y. Song, and S. Fan, Engineering arbitrarily oriented spatiotemporal optical vortices using transmission nodal lines, *Optica* **8**, 966 (2021).

[20] A. Bekshaev, Spatiotemporal optical vortices: principles of description and basic properties, *APL Photonics* **9**, 110806 (2024).

[21] N. Jhajj, I. Larkin, E. W. Rosenthal, S. Zahedpour, J. K. Wahlstrand, and H. M. Milchberg, Spatiotemporal optical vortices, *Phys. Rev. X* **6**, 031037 (2016).

[22] A. Chong, C. Wan, J. Chen, and Q. Zhan, Generation of spatiotemporal optical vortices with controllable transverse orbital angular momentum, *Nat. Photon.* **14**, 350 (2020).

[23] S. W. Hancock, S. Zahedpour, A. Goffin, and H. M. Milchberg, Free-space propagation of spatiotemporal optical vortices, *Optica* **6**, 1547 (2019).

[24] Y. Zang, A. Mirando, and A. Chong, Spatiotemporal optical vortices with arbitrary orbital angular momentum orientation by astigmatic mode converters, *Nanophotonics* **11**, 745 (2022).

[25] R. Martín-Hernández, G. Gui, L. Plaja, H. C. Kapteyn, M. M. Murnane, C.-T. Liao, M. A. Porras, and C. Hernández-García, Extreme-ultraviolet spatiotemporal vortices via high harmonic generation, *Nat. Photonics* **19**, 817 (2025).

[26] H. Zhang, Y. Sun, J. Huang, B. Wu, Z. Yang, K. Y. Bliokh, and Z. Ruan, Topologically crafted spatiotemporal vortices in acoustics, *Nat. Commun.* **14**, 6238 (2023).

[27] H. Ge, S. Liu, X.-Y. Xu, Z.-W. Long, Y. Tian, X.-P. Liu, M.-H. Lu, and Y.-F. Chen, Spatiotemporal Acoustic Vortex Beams with Transverse Orbital Angular Momentum, *Phys. Rev. Lett.* **131**, 014001 (2023).

[28] Z. Che, W. Liu, J. Ye, L. Shi, C. T. Chan, and J. Zi, Generation of Spatiotemporal Vortex Pulses by Resonant Diffractive Grating, *Phys. Rev. Lett.* **132**, 044001 (2024).

[29] M. A. Porras, Clarification of the transverse orbital angular momentum of spatiotemporal optical vortices, *J. Opt.* **26**, 095601 (2024).

[30] N. Tripathi, S. W. Hancock, and H. M. Milchberg, Transverse orbital angular momentum of spatiotemporal optical vortices: setting the record straight, *Opt. Express* **33**, 41766 (2025).

[31] T. Gadeyne and T. Ruchon, Energy and photon centroids of spatiotemporal light pulses and consequences for their intrinsic orbital angular momentum, *Phys. Rev. A* **112**, 043519 (2025).

[32] M. A. Alonso and G. W. Forbes, Uncertainty products for nonparaxial wave fields, *J. Opt. Soc. Am. A* **17**, 2391 (2000).

[33] Y. A. Kravtsov, Two new asymptotic methods in the theory of wave propagation in inhomogeneous media, *Sov. Phys. Acoust.* **14**, 1 (1968).

[34] M. V. Berry and K. E. Mount, Semiclassical approximations in wave mechanics, *Rep. Prog. Phys.* **35**, 315 (1972).

[35] S. Huang, P. Wang, Y. Xu, J. Liu, and R. Li, Fractional spatiotemporal optical vortices, arXiv:2504.11697 10.48550/arXiv.2504.11697 (2025).

[36] M. V. Berry, Optical vortices evolving from helicoidal integer and fractional phase steps, *J. Opt. A: Pure Appl. Opt.* **6**, 259 (2004).

[37] J. Leach, E. Yao, and M. J. Padgett, Observation of the vortex structure of a non-integer vortex beam, *New J. Phys.* **6**, 71 (2004).

[38] K. Y. Bliokh and F. Nori, Relativistic Hall Effect, *Phys. Rev. Lett.* **108**, 120403 (2012).

[39] S. W. Hancock, S. Zahedpour, A. Goffin, and H. M. Milchberg, Spatiotemporal Torquing of Light, *Phys. Rev. X* **14**, 011031 (2024).

[40] K. Y. Bliokh, On the Ehrenfest theorem and centroids of relativistic particles, *Phys. Lett. A* **542**, 130425 (2025).

Appendix A: Centroids and OAM expressions in the nonparaxial regime

The following tables show the expressions for the centroids and OAM calculated with Eqs. (6), (8), and (9) from the main document. Here, E and K designate respectively the complete elliptic integrals of the second and first kinds, and Δ_x was replaced by $\tan \eta$, where η designates the maximum ray angle in the ray family.

TABLE VI. Nonparaxial regime for an xz STVP

Quantity	
x_{cent}	0
$x_{0\text{min}}$	$-w_z \tan \frac{\eta}{2}$
$\langle L_y \rangle(x_{\text{cent}})$	$-2w_z \left[\frac{1}{\tan \eta} E(-\tan^2 \eta) - \frac{1}{\tan \eta} K(-\tan^2 \eta) + \left(\frac{1}{\sin \eta} E(\sin^2 \eta) - \cos^2 \eta K(\sin^2 \eta) \right) \right]$
$\langle L_y \rangle(x_{0\text{min}})$	$-2w_z \left[\frac{1}{\tan \eta} E(-\tan^2 \eta) + \left(\frac{2}{\tan \eta} - \frac{1}{\sin \eta} \right) K(-\tan^2 \eta) + \left(\frac{1}{\sin \eta} E(\sin^2 \eta) + \cos \eta \left(\frac{2}{\tan \eta} - \frac{1}{\sin \eta} \right) K(\sin^2 \eta) \right) \right]$

TABLE VII. Nonparaxial regime for an xt STVP

Quantity	
x_{cent}	$-\frac{2w_t}{\tan \eta} \left[E(-\tan^2 \eta) - K(-\tan^2 \eta) + \left(\frac{1}{\cos \eta} E(\sin^2 \eta) - \cos \eta K(\sin^2 \eta) \right) \right]$
$x_{0\text{min}}$	0
$\langle L_y \rangle(x_{\text{cent}})$	$-2x_{\text{cent}} \left[K(-\tan^2 \eta) + \cos \eta K(\sin^2 \eta) \right]$
$\langle L_y \rangle(x_{0\text{min}})$	0

Appendix B: Solutions for the phase

The phase $\Phi(\xi)$ is meant to ensure that all ray contributions are added in phase. Equation (10) from the main document can be integrated both for xz and xt STVPs. By choosing the condition $\Phi(0) = 0$, we find for the xz STVPs:

$$\begin{aligned} \Phi(\xi) = k_0 w_x & \left[\frac{\sqrt{1 + \Delta_x^2}}{\Delta_x} E\left(\xi, \frac{\Delta_x^2}{1 + \Delta_x^2}\right) - \frac{1}{\Delta_x \sqrt{1 + \Delta_x^2}} F\left(\xi, \frac{\Delta_x^2}{1 + \Delta_x^2}\right) \right] \\ & + k_0 w_z \log\left(\frac{\sqrt{2}\Delta_x \cos \xi + \sqrt{2 + \Delta_x^2 + \Delta_x^2 \cos 2\xi}}{\sqrt{2}\Delta_x + \sqrt{2 + 2\Delta_x^2}}\right), \end{aligned} \quad (B1)$$

and for xt STVPs:

$$\begin{aligned} \Phi(\xi) = k_0 w_t & (\cos \xi - 1) \\ & + k_0 w_x \left[\frac{\sqrt{1 + \Delta_x^2}}{\Delta_x} E\left(\xi, \frac{\Delta_x^2}{1 + \Delta_x^2}\right) - \frac{1}{\Delta_x \sqrt{1 + \Delta_x^2}} F\left(\xi, \frac{\Delta_x^2}{1 + \Delta_x^2}\right) \right], \end{aligned} \quad (B2)$$

where F and E are, respectively, the elliptic integrals of the first and second kinds. As a consequence, the integrand of Eq. (12) in the main document can be expressed in an analytical form in both cases. Notice that both equations (B1) and (B2) define similar functions that only differ in one term.

The choice of the parameters w_x , w_z (or w_t), and Δ_x allows tailoring the shape of the pulse. As mentioned in the main text, the integral in ξ should be independent of the choice of limits as long as the interval covers the complete

loop. This means that the integrand must be a periodic function of ξ , which is only true if $\Phi(2\pi) = 2\pi\ell$ where the integer ℓ corresponds to the STVP's topological charge. For both types of STVP, this leads to the same constraint:

$$\frac{4k_0w_x}{\Delta_x} \left[\sqrt{1 + \Delta_x^2} E\left(\frac{\Delta_x^2}{1 + \Delta_x^2}\right) - \frac{1}{\sqrt{1 + \Delta_x^2}} K\left(\frac{\Delta_x^2}{1 + \Delta_x^2}\right) \right] = 2\pi\ell, \quad (\text{B3})$$

where K and E are, respectively, the complete elliptic integral of the first kind and the complete elliptic integral.

The paraxial regime can be studied by approximating the expressions of $\Phi(\xi)$ of Eqs. (B1) and (B2). By an expansion in Δ_x up to the second order, we find for the xz STVPs:

$$\begin{aligned} \Phi(\xi) \simeq k_0w_z (\cos \xi - 1) &+ \frac{k_0\Delta_x}{4} [w_z + 2w_x\xi - 2w_z \cos^2 \xi + w_z \cos(2\xi) + w_x \sin(2\xi)] \\ &+ \frac{k_0w_z\Delta_x^2}{12} (2 - 3 \cos \xi + 4 \cos^3 \xi - 3 \cos \xi \cos(2\xi)], \end{aligned} \quad (\text{B4})$$

and for the xt STVPs:

$$\Phi(\xi) \simeq k_0w_t (\cos \xi - 1) + \frac{\Delta_x}{4} k_0w_x (2\xi + \sin 2\xi). \quad (\text{B5})$$

The constraint is again the same in both frameworks:

$$\Phi(2\pi) = k_0\pi w_x \Delta_x = 2\pi\ell. \quad (\text{B6})$$